water

MDPI

Article

Hydrologic Impact of Climate Change in the Jaguari River in the Cantareira Reservoir System

Leonardo Moreno Domingues [1,2,*], Rafael Cesario de Abreu [1] and Humberto Ribeiro da Rocha [1]

1 Instituto de Astronomia, Geofísica e Ciências Atmosféricas, Universidade de São Paulo, Rua do Matão, 1226, Cidade Universitária, São Paulo 05508-090, Brazil; rafael.abreu@iag.usp.br (R.C.d.A.); humberto.rocha@iag.usp.br (H.R.d.R.)
2 Coordenação de Dinâmica Ambiental, Instituto Nacional de Pesquisas da Amazônia, Manaus 69067-375, Brazil
* Correspondence: leomdomingues@gmail.com

Abstract: A recent drought in Southeast Brazil affected the Cantareira reservoirs system (CRS), which supplies water to São Paulo megacity, and raised concerns on the impacts that climate change may have on the water budget at the watershed scale. We propose to identify the particular and summed contributions of key climatic variables on the variability of the water budget in Jaguari basin, the main CRS tributary, using forcing–response relationships derived from climate projections and individual elasticities of variables to temperature. Besides, we investigated whether hydrological effects of the anomalous drought were comparable to patterns simulated in the future climate. A thoroughly calibrated hydrological model for evapotranspiration (ET) and discharge (Q) was used to address our questions. We found opposite impacts in the future mostly driven by rainfall changes: under increasing (decreasing) rainfall, the mean ET increased (decreased) up to +25% (−10%) and Q increased (decreased) by +90% (−50%). Higher carbon dioxide concentrations strongly depleted the stomatal conductance, and thus the mean ET, which in turn increased the mean Q in near proportions. Major critical impacts for water management are suggested by the results. Even with a small reduction of precipitation, the discharge patterns in the drought event were replicated at similar intensities.

Keywords: Cantareira; climate change; water budget; drought

check for updates

Citation: Domingues, L.M.; de Abreu, R.C.; da Rocha, H.R. Hydrologic Impact of Climate Change in the Jaguari River in the Cantareira Reservoir System. *Water* **2022**, *14*, 1286. https://doi.org/10.3390/w14081286

Academic Editor: Maria Mimikou

Received: 18 February 2022
Accepted: 11 April 2022
Published: 15 April 2022

1. Introduction

The Cantareira reservoirs system (CRS) in Southeast Brazil supplies about nine million people in São Paulo city. After an above-normal rainfall and water volume peaking period in 2009/2010, the CRS was affected by successive years with decreasing rainfall volume, which reached criticality in 2014, mostly as a response to the outstanding 2013/2014 drought [1]. The precipitation decreased by about 44% during the regional drought in 2014 [1], and the summer temperature was the highest since 1951, which must have also contributed to increased water losses such as land evapotranspiration, open water reservoir evaporation, and water withdrawals due to the overall consumption [2,3]. The scarcity at the CRS pushed a substantial water shortage at the regional scale, especially in São Paulo city, where a suite of management measures was taken, including pressure reduction in water pipes and the reduction of industrial/domestic consumption [4]. Despite allusions that the drought could have been attributed to global climate change [5], the comprehensive work of Otto et al. [6] did not find significant evidence to confirm this hypothesis, but rather, a natural phenomenon. Authors in general considered the drought as an exceptionality [1,2,6], with a return period of 98 years [3].

Hydrological droughts are expected to become more intense and frequent as the atmosphere becomes warmer in most regions of South America, including Southeast Brazil [7]. In megacities such as São Paulo, climate change may add an additional pressure regarding its impacts on droughts, or more broadly, on water security. While the global urban population facing water scarcity was 933 million in 2016, it is expected to increase to up to 2.373 billion people in 2050 [8].

Assessing the impacts of climate change on the surface water budget at regional scales requires substantial improvements over coarse-scale climate projections. The sensitivity of land hydrology to climate change projections is commonly addressed with physically based hydrological models (HMs). These models take advantage of solving biophysical processes at high spatial resolution, such as evapotranspiration (ET), soil moisture, and water flows, and depend on local characteristics, such as topography and land cover [9]. Sensitivity can be also addressed with simple Budyko-type models that combine temperature, radiation, and ET [10,11]. Besides rainfall and temperature, other climatic variables such as vapor pressure deficit (vpd), carbon dioxide (CO_2) concentration, and solar radiation are well-known controls of ET that consequently affect the mean discharge (Q) at the catchment scale.

The high confidence in the temperature increase in future climate projections expects increasing saturated vapor pressure in the lower troposphere [12]. Byrne and O'Gorman [13] suggested that the increase in saturation-specific humidity surpasses other contributions that add moisture from oceanic source transports and land ET, which would reduce the land relative humidity (RH) and increase both vpd and potential evapotranspiration (PET). Guo et al. [14] reported that the Food and Agriculture Organization of the United Nations Penman–Monteith PET in humid catchments was more sensitive to temperature, followed by RH, whereas solar radiation and wind speed played minor roles; however, they did not include CO_2 controls explicitly. The authors showed that stomatal conductance (g_s) decreases in both C3 and C4 plants under increasing CO_2 concentration [15,16], which suppresses transpiration [16–18] and can increase soil water content and runoff [17,19,20].

A common framework to investigate the impacts of climate change in regional land hydrology is by selecting one or more scenarios of the International Panel on Climate Change (IPCC) and choosing one or more general circulation model (GCM) projections [21]. Then, bridging the gap between GCMs and HMs becomes crucial [22,23], and coarse-resolution GCM data should be treated to obtain an unbiased and finer resolution at regional watershed scales, often accomplished with dynamical or statistical downscaling. Finally, HMs need calibration performed under accurate and long-term historical climate and discharge observations, which is supposed to work properly in future climates (see, for instance, [24,25]). Di Baldassarre et al. [21] also emphasized a great dependence of climate projections on the emission scenarios and anthropogenic activities, which in turn are changing over the years. In the IPCC Fourth Assessment Report, the projections were based on the Special Report on Emissions Scenarios [26], followed by Representative Concentration Pathways (RCPs) [27] in the Fifth Assessment Report, and more recently on Shared Socioeconomic Pathways [28], which make comparisons among scenarios of different generations difficult to assess. Alternatively, other authors (e.g., [29,30]) addressed the question of understanding the rate of climate forcing and the rate of hydrological response using pattern-scaling relationships, where each forcing climate variable of the HM is assumed to respond linearly to the changing mean annual temperature.

In Southeast Brazil, global projections agree that mean temperature may increase up to 5 °C under the RCP 8.5 scenario in the late 21st Century, but the projected changes of rainfall are diverging and show either higher or less precipitation than the historical period [31]. To address the diverging issues, this work approached a sensitivity study comprehending the whole range of significant impacts, based on the concept of the elasticity of key climate variables to air temperature. The main advantages of the elasticity are: (i) avoiding the many steps involving impact assessment, such as climate model choice, downscaling, and bias correction, among others, which also present many sources of cumulative errors in each step; (ii) easily matching the simulated variability on water fluxes to changes in the forcing data.

The elasticity accounts for the percentage or absolute change of a variable in response to a change in another. For instance, Held and Soden [12] reported that the absolute elasticity of precipitable water to temperature increase from climate change projections for the late 21st Century was 7.5% °C^{-1} and, similar to precipitation, 2.2% °C^{-1}. Using the physically based semi-distributed Soil Water Assessment Tool (SWAT) model with a thorough calibration for both ET and Q, we designed a strategy using forcing–response relationships to estimate the impact of climate change in the surface water budget over the Jaguari river basin, the main affluent of the CRS. We aimed to identify the particular and summed contribution of key climatic variables (temperature, rainfall, air humidity, and CO_2 concentration) on the variability of the land water budget in historical and future time slices. Specially, we addressed a second question, whether the hydrological effects of the exceptionally anomalous 2014 drought are comparable to the patterns simulated in the future climate.

2. Materials and Methods

2.1. Study Area

The CRS is a group of reservoirs, tunnels, and channels that divert water from the Piracicaba river basin to the Upper Tietê river basin, composed by the reservoirs of the Jaguari-Jacareí, Cachoeira, and Atibainha rivers, with the purpose of supplying the Metropolitan Area of São Paulo city in Southeast Brazil (Figure 1a) [32].

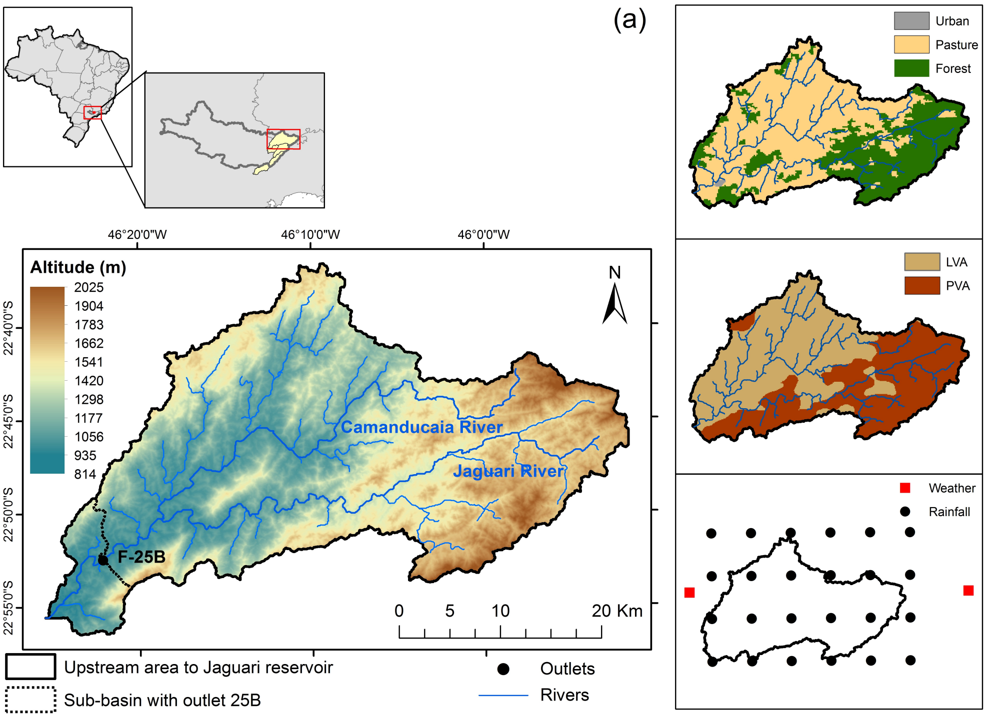

Figure 1. (**a**) Altitudinal map of the Jaguari river basin (m) with the outflow at gauge station F-25B (22.875° S and 46.369° W) within the Piracicaba river basin (grey shaded picture at top) and upstream the CRS (yellow shaded area at top). (**b**) Land use map; (**c**) soil map, where soil types LVA and PVA are Red-Yellow Latosol and Argisol, respectively; (**d**) location of rainfall (black circles) and weather (red squares) data.

2.2. SWAT Model Description and Setup

SWAT is a semi-distributed, continuous-time model, which represents processes from small to large basin scales, on daily time steps, to assess the impacts of management on yields of water, sediments, and agricultural chemical components [33]. The model is called semi-distributed because a given watershed is initially divided into sub-basins, according to the topography, and then divided into hydrological response units (HRUs), which are areas of common slope class, soil, and land use. The water balance is solved within each HRU domain, computing individual processes in the vadose zone and shallow aquifer (e.g., surface, lateral and base flows, transpiration, soil evaporation, water seepage), as well as the intercepted water in the canopy and deep aquifer recharge. The HRU-scale water flow is then aggregated and routed in the drainage network. For more details, the reader is referred to Neitsch et al. [34].

We used the ArcSWAT 2012.10.2.18 extension, via ArcGIS® 10.2.2, to build the boundary conditions and the SWAT 2012 rev. 591 version to perform our simulations. Details are summarized in Table 1.

Table 1. Description of maps and data used in the setup of boundary conditions.

	Reference	Resolution
Digital elevation map	ASF DAAC [35]	12.5 m
Land use map	IBGE [36]	12.5 m
Soil map	UFV-CETEC-UFLA-FEAM [37]	12.5 m
Weather data	ERA-Interim [38]	≈79 km
Rainfall data	Inverse distance weighting [39] from available gauges	10 km

Both land use and soil maps were adapted to simplify the representation of classes in the watershed and were converted from original vector files to the Digital Elevation Model resolution. According to the MapBiomas project [40], forested (sum of forest formation and artificial forests classes) and pastured (sum of pasture, mosaic of pasture and agriculture, and other temporary crops classes) areas varied between 43 and 47% and 50 and 55%, respectively, of the total Jaguari area during 1995–2017. For this reason, it seemed reasonable to maintain a unique land use map for the entire period. The soil physical properties were initially set according to Pontes et al. [41], and further adjustments are described in Appendix B. With respect to the weather data, it includes maximum and minimum temperatures (°C), wind speed (m s^{-1}), and relative humidity and solar radiation (MJ m^2 d^{-1}), while rainfall (mm d^{-1}) is an interpolated product of available gauges in the basin. We used gauges from the National Water Agency, Basic Sanitation Company of the State of São Paulo, National Center for Monitoring and Early Warning of Natural Disasters, Brazilian National Institute of Meteorology and Agronomic Institute of Campinas, after a careful review.

We set the CO_2 concentration based on observed mean global temporal rates during the range of time [42], starting from 350 ppm and increasing at approximately 2 ppm per year.

2.3. Calibration

We used gauge station F-25B [43] as the reference to calibrate Jaguari river discharge. This gauge sums 94% (965.7 km^2) of the contribution area to the Jaguari reservoir (Figure 1) and has a mean discharge of 19 m^3 s^{-1}. Quality control removed gross errors with visual inspection and comparison with close gauges. The period 2003–2017 was selected for calibration due to its greater interannual variability than 1995–2002, which was used for validation. A warm up period of 5 years was taken for both calibration (1998–2002) and validation (1990–1994). We first prescribed parameter values based on the literature [41,44–46] to run the Particle Swarm Optimization algorithm from SWAT-CUP [47], in order to assess the most sensitive parameters. A fine-tuning process of calibration was applied with the swatplusR 0.2.7 package [48] running in R [49]. Latin Hypercube Sampling (LHS) was used to produce a 2000-length distribution of 15 parameters to be calibrated (selected from the previous step). Then, a SWAT output was taken out of the 2000 possibilities, and the simulated discharge was evaluated using the Nash–Sutcliffe efficiency (NSE) index. The simulation presenting the best NSE index was then used for the validation period.

2.4. Experimental Design of Perturbations in Climatic Forcings

The elasticity $\epsilon_{z,x}$ addresses how much a percentage change $\frac{dz}{\overline{z}}$ (of a variable z) responds to another percentage change $\frac{dx}{\overline{x}}$ (of a variable x), where $\overline{z}$ and $\overline{x}$ are temporal averages, respectively, and simply accounts for the result of changing a variable as a function of changes in another one. In this work, the experimental design used the elasticity of key atmospheric variables (precipitation and air humidity) to near-surface air temperature. The temporal changes of mean rainfall (P) and specific humidity (q) were accounted upon the correspondent changes of air temperature (T), defined as the elasticities $\epsilon_{P,T}$ and $\epsilon_{q,T}$, respectively, that represented the percentage of change in P (or q) per 1 °C change of temperature, as follows:

$$\epsilon_{P,T} = \frac{1}{\overline{P}} \frac{\Delta P}{\Delta T} \quad (1)$$

$$\epsilon_{q,T} = \frac{1}{\overline{q}} \frac{\Delta q}{\Delta T}, \quad (2)$$

where ΔP, ΔT, and Δq are temporal changes of P, T, and q, respectively, and $\overline{P}$ and $\overline{q}$ are the mean values of P and q, all calculated over a prescribed range of time.

We used the estimates of Equations (1) and (2) calculated with climate simulations of 37 models (ACCESS1.0, ACCESS1.3, BNU-ESM, CCSM4, CESM1-BGC, CESM1-CAM5, CESM1-WACCM, CMCC-CESM, CMCC-CM, CMCC-CMS, CNRM-CM5, CSIRO-Mk3.6.0, CanESM2, FGOALS-g2, GFDL-CM3, GFDL-ESM2G, GFDL-ESM2M, GISS-E2-H, GISS-E2-H-CC, GISS-E2-R, GISS-E2-R-CC, HadGEM2-CC, HadGEM2-ES, IPSL-CM5A-LR, IPSL-CM5A-MR, IPSL-CM5B-LR, MIROC-ESM, MIROC-ESM-CHEM, MIROC5, MPI-ESM-LR, MPI-ESM-MR, MRI-CGCM3, NorESM1-M, NorESM1-ME, BCC-CSM1.1, BCC-CSM1.1(m), and INM-CM4) of the Coupled Model Intercomparison Project—Phase 5 (CMIP5, [50]). We first interpolated the GCM outputs to a common 0.5° × 0.5° horizontal resolution grid, and the ensemble mean of each model was calculated over a grid box centered in Southeast Brazil. Then, we calculated the simple difference of an average variable in the future climate (2075–2099) minus the average in the historical period (1980–2004) to account for temporal changes and mean long-term values for the entire period (1980–2099) in Equations (1) and (2), retaining only statistically significant differences of a p-level of 5%. For the future climate, we used RCP 8.5 ensembles that usually constrained a higher CO_2 concentration (and also higher temperatures) out of other scenarios at the end of the 21st Century. This scenario was selected deliberately in order to obtain the highest signal-to-noise ratio responses to increasing CO_2.

For the elasticity analysis, we assumed linear relationships between T and P and T and q. The residue of the linear fit between $T \times P$ and $T \times q$ was calculated, and the Kolmogorov–Smirnov normality test was applied to each climate model. We found that 91% and 92% of the models, for humidity and rainfall, respectively, presented residues following a normal distribution, allowing the use of a linear fit for this analysis.

Figure 2a shows the spread of the mean annual air temperature of all CMIP5 models, from historical to future climate time slices used here, wherein most projections showed an increase from 3 to 4.5 °C (Figure 2b). The variability of $\epsilon_{P,T}$ was higher than $\epsilon_{q,T}$ over the models (two upper rows in Figure 2c). We noted a systematic increase in specific humidity with the temperature ranging up to 10% °C^{-1}, and for precipitation, the patterns varied from decreasing to increasing changes, ranging from about −10 to +20% °C^{-1}, respectively. These patterns in precipitation, in general, agreed with previous reports [31]. Besides, the elasticities of ET and (P-ET) (two bottom rows in Figure 2c) varied from −5 to 5% °C^{-1} for ET with a positive average though, and for (P-ET), a wider range from about −20 to 20% °C^{-1} was shown. Such estimates of (P-ET) elasticities varying from a substantial increase to decrease emphasize the lack of consensus about land water availability as provided by global models. However, it is important to note that the higher variability of

(P-ET) was also due to the percentage calculation, which tends to inflate smaller absolute values. We stress that, since elasticity accounts for the temporal rates of temperature, the absolute changes tend to increase in the future climate. For example, $\epsilon_{P,T}$ = 10% °C^{-1} suggests a modest 10% increase in rainfall (associated with a 1 °C warmer temperature), although it leads to a 30% increase of rainfall in a 3 °C warmer climate and likewise, for $\epsilon_{P,T}$ = 20% °C^{-1}, a 60% increase of rainfall for the same 3 °C warmer climate. However, the probabilities of the rainfall elasticity among the set of models were different, wherein highest and lowest elasticities are less likely, though significant.

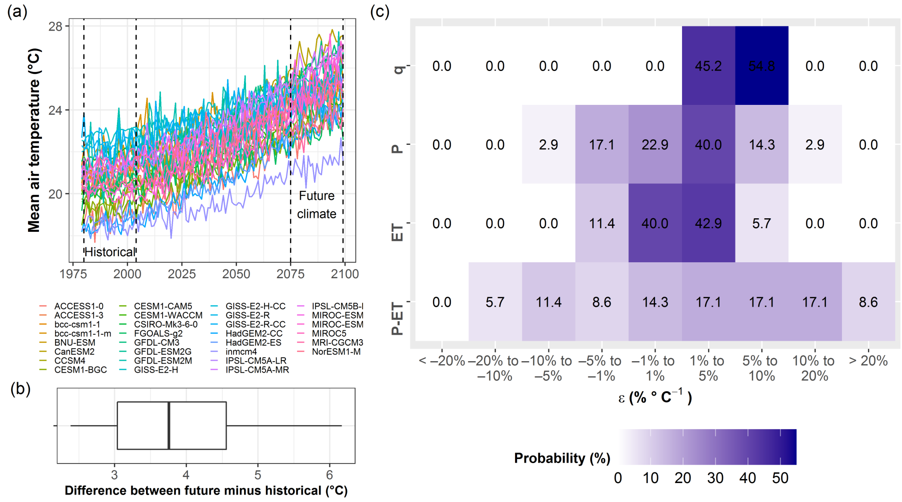

Figure 2. (**a**) Mean annual air temperature (°C) projected by CMIP5 climate models from 1980 to 2099; (**b**) boxplot of the difference between future minus historical time slices of mean air temperature (°C); (**c**) probabilities of occurrence (%) of elasticity to temperature for precipitation (P), specific humidity (q), evapotranspiration (ET), and precipitation minus evapotranspiration (P-ET), in % °C^{-1}.

The Set of Experiments

We chose the 23 years of weather data (1995–2017) used for model calibration/validation as the reference forcing data to simulate the hydrological outputs, here referred to as the control experiment. Upon that, we defined case-specific perturbations on key forcing variables (air temperature, humidity, precipitation, and CO_2 concentration) to design the experiments.

Firstly, for the temperature, we defined 5 cases of varying temperature, with perturbations prescribed as changes in mean daily air temperature (T_{av}) from +1 to +5 °C above the control, each case, respectively. The SWAT model was forced with maximum and minimum temperatures, so both variables were simply offset accordingly to each perturbation case. The changes with respect to control case distribution are shown in Figure 3a.

Second, for air relative humidity (RH), we defined 3 cases with perturbations based on the $\epsilon_{q,T}$ variability derived from the CMIP variability (Figure 2c): $\epsilon_{q,T}$ = 5, 7.5, and 10% °C^{-1}, respectively. With the control case RH and T_{av}, we calculated the water vapor pressure $e = e_s \cdot \mathrm{RH}$, where e_s is the saturated water vapor pressure, exclusively dependent on T_{av}. Then, e_s is updated to the case-specific temperature increase (+1 to +5 °C), e is incremented at the 3 percentages of $\epsilon_{q,T}$, and RH cases are calculated. The prescribed perturbations in the control RH show that they conveniently represented variations in the distribution (Figure 3b) with reduced, alike, and increased RH cases when compared to the control, for elasticities of 5, 7.5, and 10% °C^{-1}, respectively. As the alike case incidentally compared well with the control case (gray and green curves in Figure 3b), it is suggested that to keep RH approximately constant with increasing temperature required a 7.5% increase of specific humidity per °C of temperature change. Furthermore, we made some simplifications: for $\epsilon_{q,T}$ = 10 °C, a few cases exceeded RH a little beyond 100%, in particular for higher temperature increases, which we limited to 100% to keep consistency. Based on the comparison to the RH control case, in summary, we refer to the three cases as lower RH (5% °C^{-1}), alike RH (7.5% °C^{-1}), and higher RH (10% °C^{-1}), respectively.

Third, for precipitation, we defined four cases with perturbations based on $\epsilon_{P,T}$ variability (Figure 2c): -5, 0, 5, and 10% °C^{-1}, which totaled 94.3% of all probabilities. The rainfall was changed by simple scaling of every daily rainfall episode of the control case to percentages according to the four aforementioned cases and to case-specific temperature increases (+1 to +5 °C). The distributions of daily precipitation depicted in the elasticity cases are shown in Figure 3c. The less precipitation forcing increased (decreased) the distribution below (above) 10 mm d^{-1} with respect to $\epsilon_{P,T}$ = 0% °C^{-1}, and events above 100 mm d^{-1} were not quantified. In general, the cases with $\epsilon_{P,T}$ = 5 and 10% °C^{-1} presented the opposite pattern: less events with P < 10 mm d^{-1} and more with P > 10 mm d^{-1} than the control case; the $\epsilon_{P,T}$ = 10% °C^{-1} case reached events up to 150 mm d^{-1}.

Finally, to alter the CO_2 concentration, we defined perturbations in two cases (Figure 3d): the first with prescribed daily time series as used in the calibration, here referred to as the historical case; the second based on the projected temporal rates for the RCP 8.5 during 2075–2099 [27], which started at 750 ppm and increased at 8 ppm per year, referred to as the end of the century case.

The incoming solar radiation and ground wind speed variables, despite being key model forcings that control ET, were chosen not to be altered in our experiments, helping to keep the design simpler.

The perturbations in temperature, humidity, and rainfall time series were performed prior to SWAT simulations, in an independent process. Differently, the CO_2 concentration was manually added to the SWAT source code as linear equations, as shown in Figure 3d.

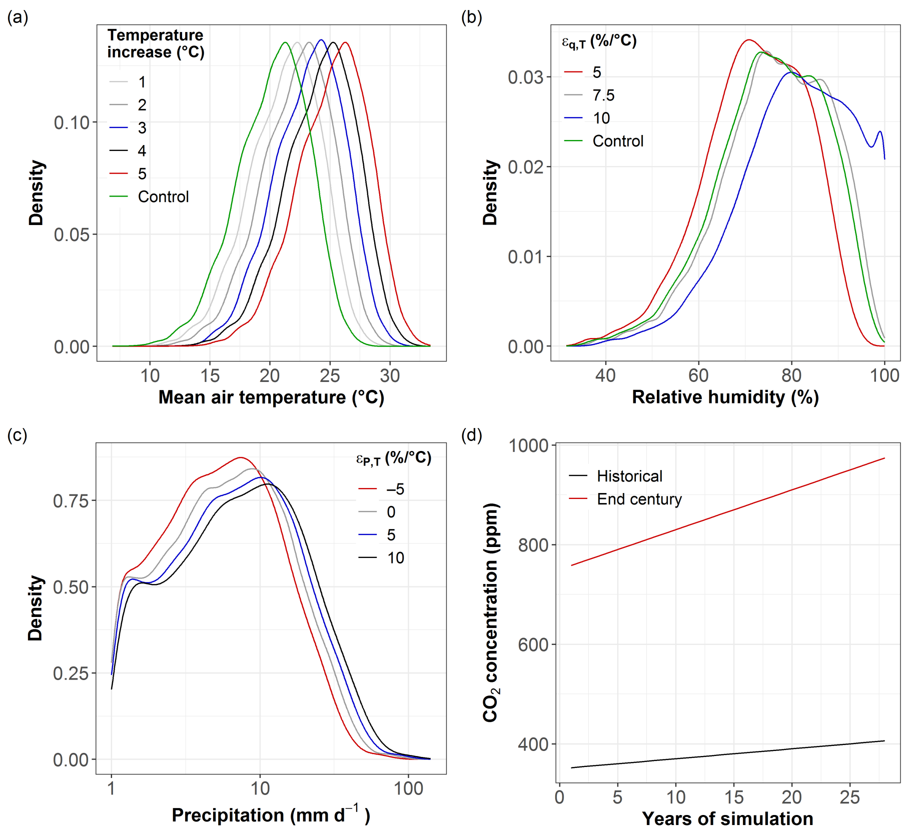

Figure 3. Density plot of (**a**) mean air temperature, in °C; (**b**) relative humidity, in %; and (**c**) precipitation, in mm d^{-1}. Colors differentiate, respectively, the increase in temperature, $\epsilon_{q,T}$ and $\epsilon_{P,T}$ cases. (**d**) CO_2 concentration over the years of simulation, in ppm, for historical (black line, y $=$ 350 $+$ 2x) and end of the century (red line, y $=$ 750 $+$ 8x) conditions.

In summary, we ran a set of 120 simulations plus a control case, using the calibrated model, each one spanning a 28-year range of time, which combined the specific cases of air temperature (five cases), precipitation (four cases), air relative humidity (three cases), and air CO_2 concentration (two cases). A flowchart summarizing the processes in our experiment design is shown in Figure 4.

The impacts are discussed with outputs for key hydrological variables, based on averages of each simulation during the 28-year range, which were partly assessed during the last 23 years (first 5 years were taken as the warm up for soil moisture).

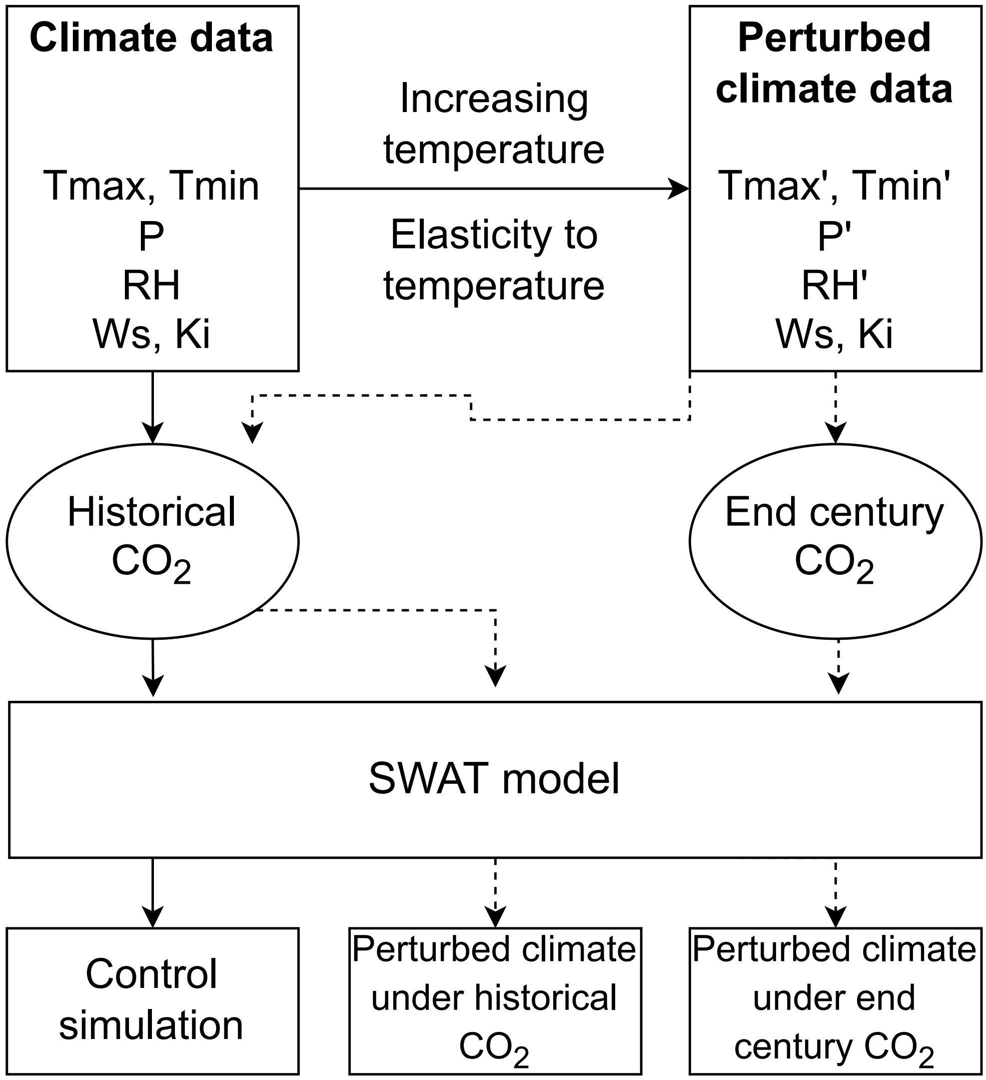

Figure 4. Flowchart of the experiment design. Abbreviations Tmax, Tmin, P, RH, Ws, and Ki refer to maximum air temperature, minimum air temperature, relative humidity, wind speed, and incoming solar radiation.

3. Results and Discussion

3.1. Model Calibration

We firstly proceeded with a thorough inspection of the ET calculations before the discharge calibration and opted for altering specific ET model parametrizations to help improve the experiments. It was noted that the previously calculated ratio of soil evaporation to ET (=transpiration + soil evaporation + interception loss) tended to be overestimated when compared to typical values for the prescribed land cover types (not shown) of subtropical humid forest (max ≈ 10%) and managed pasture (max ≈ 25%). In addition, the time-variant leaf area index (LAI) parameter, which controls transpiration and rain interception, did not show a consistent typical magnitude nor seasonality, as previously noted by Strauch et al. [44]. The alterations were proceeded in specific control parameters of soil evaporation and soil moisture retention at the top soil layer, maximum stomatal conductance, rooting depth, and LAI temporal dynamics (see Appendix A). The achievements were key to better simulate the ET components' partition, which is believed to help simulate properly the impacts of changing rainfall, temperature, vpd, and CO_2 concentration differently for transpiration and other terms in future climate experiments.

Regional ET products are available by ET-satellite models [51,52], reanalysis [38], land surface model [53], field water budget [54,55], and field eddy covariance measures [56], which vary according to case-specific spatio-temporal scale data and accuracy. We used the terrestrial water balance (TWB) approach using monthly field precipitation (*P*) and specific discharge (Q) and terrestrial water storage (TWS) from the GRACE satellite/CSR RL05 Mascon product (2003–2011) [57] as a proxy to soil water storage variation. The annual TWB provides a direct regional ET estimate and is about to be the more appropriate reference to compare this case study. In general, the mean monthly model calculated ET compared well the TWB (Figure 5). During the early dry season around May (Figure 5a), an atypical oscillation of TWB time series disagreed with the smoothed calculated ET variability. We can only suppose this oscillation as evolving from the TWS coarse resolution data and the large temporal variance of the TWB (Figure 5b). The mean seasonal calculated ET agreed with the TWB, which showed differences of less than 0.2 mm d^{-1} (Figure 5b).

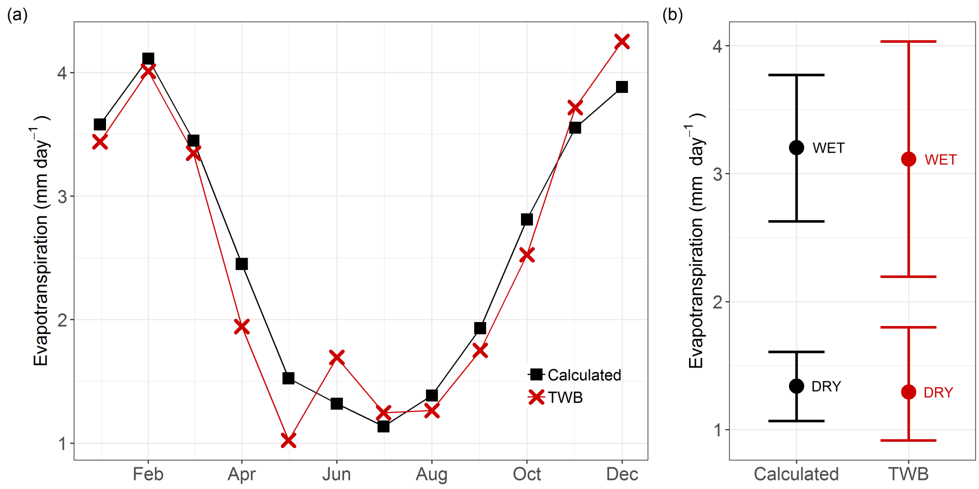

Figure 5. (**a**) Mean monthly ET, in mm d^{-1}, calculated by the model (black squares) and estimated by TWB (red crosses). (**b**) ET average (points) and 75th and 25th percentiles (bars), in mm d^{-1}, for each estimate in dry (May to Aug) and wet (Sep to Apr) seasons. Panels use the common period for model and TWB.

For the discharge calibration, we tested the null hypothesis (two-sample *t*-test plev-5%) that a given parameter does not modify the NSE index, by combining all indexes and parameters, which worked as a sensitivity analysis. The hypothesis was rejected for all parameters except GW_DELAY, HRU_SLP, SLSUBBSN, CN2, and GWQMN (see the set of parameters, range of variation, and default/best values in Table A3). Despite not being sensitive in this analysis, these parameters contributed to maximizing the NSE index. The performances of calibration and validation for discharge showed NSE indexes of 0.82 and 0.85, respectively, evaluated as very good [58]. The calculated discharge was, in general, consistent with the observations (Figure 6b,c). The model showed a tendency to underestimate some observations, e.g., the higher peaks in the validation runs (Figure 6c). Besides being a very traditional goodness-of-fit criteria in hydrologic studies, the NSE is commonly reported to have a lower performance on low flows (see, for instance, [59,60]). It happens essentially due to the squared difference between observed and predicted values, which turns the NSE oversensitive to peak flows. In addition, as described by

Zheng et al. [61], when extreme events are included in the calibration process, as in our study, the model development is influenced by such conditions and tends to perform worse than under normal conditions. In such cases, the validation would present better performance than if it had the inclusion of extremes. This issue probably explains the better performance on validation than calibration in this study. Furthermore, the calibration was influenced by lower-than-average discharge data, so that the model slightly underestimated the simulation of low flows under normal conditions, but not in the extreme cases of 2014/15 during the regional drought and onward (Figure 6b). Finally, some authors already regard the baseflow simulation as one of the main weaknesses of SWAT, due to its simplified groundwater concept [62]. Despite these aforementioned issues, ET and Q calibration were, in general, successful, with adequate modeling performance to simulate the type of proposed experiments in this work.

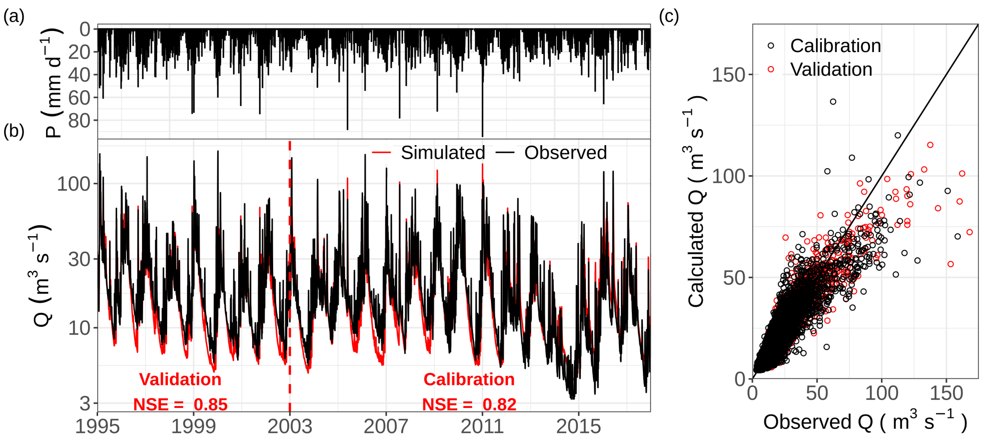

Figure 6. (**a**) Basin-averaged daily precipitation, in mm d^{-1}. (**b**) Simulated (red line) and observed (black line) discharges, in m^3 s^{-1}, with *y*-axis in log scale. Vertical dashed line separates calibration from validation, and labels show the NSE index. (**c**) Scatter plot of observed and calculated discharges, for calibration (black circles) and validation (red circles) periods.

3.2. Climate Change Impacts on ET and Q

Figure 7 shows the differences ΔET and ΔQ of experiments minus the control simulation for ET and Q, respectively, and depicts the cases of increasing temperature (abscissa), RH changes (line types), and rainfall changes (line colors with labeled changes). With the historical CO_2 case and no change in precipitation ($\epsilon_{P,T}$ = 0% °C^{-1}, grey lines), we narrowed the effects of only temperature and humidity. In such cases, regardless of the RH condition, ET generally increased nearly linearly with temperature, from about 13 to 64 mm yr^{-1} (1 to 7%) (Figure 7a), and Q reduced approximately at the same rate (Figure 7b). A lowering RH tended to enhance the increasing ET with temperature by less than 5% and, likewise, helped to decrease Q at similar deviations. These results are consistent as increased temperature and decreased RH raise the evaporative demand [63], which is explicitly part of the transpiration calculation in SWAT [34] via the vpd term. For the historical CO_2 also, we observed that with forcings of less precipitation in the future, the reductions ranged from 77 to 385 mm yr^{-1} with increasing temperature ($\epsilon_{P,T}$ = −5% °C^{-1}, red lines). ET and Q were simultaneously reduced for all RH cases with less precipitation, whereas the reductions in ET were much less than those in rainfall, from 7 to 88 mm yr^{-1} (1 to 9%), the changes in Q compared better to *P*, namely from 68 to 294 mm yr^{-1} (11 to 49%), all for the alike RH case. Additionally, the lowering RH tended to reverse the effect of the decreasing ET with temperature, though only by less than 2%.

Finally, for the historical CO_2 cases, but with higher precipitation forcing, *P* was prescribed to increase from 76 to 384 mm yr^{-1} and from 154 to 771 mm yr^{-1} for $\epsilon_{P,T}$ = 5 (blue lines in Figure 7a,b) and 10% °C^{-1} (black lines in Figure 7a,b), respectively. The responses to temperature and humidity changes showed that, for all RH cases, both ET and

Q generally increased near linearly with temperature. Regarding the responses of these two precipitation changes, ET increased up to maxima of 161 and 229 mm yr^{-1} (17 and 24%) (Figure 7a) and Q up to 218 and 530 mm yr^{-1} (36 and 88%) (Figure 7b). We attributed the lower changes in ET in comparison to Q especially to energy limitation, which was not addressed in our experiments. Similar to the $\epsilon_{P,T}$ = 0% °C^{-1} case, the comparison of higher to lower RH, e.g., with $\epsilon_{P,T}$ = 10% °C^{-1}, tended to enhance the increasing ET with temperature, up to about 50 mm yr^{-1} or 5%, and likewise, to decrease Q at similar deviations. Comparing all cases of precipitation changes, those with less precipitation forcing ($\epsilon_{P,T}$ = −5% °C^{-1}) apparently led to a pronounced soil moisture deficit, which in turn limited ET and shifted its response to decrease with increasing temperature. Differently, other cases with constant/increasing precipitation ($\epsilon_{P,T}$ = 0; 5 and 10% °C^{-1}) did not revert the increasing ET response to temperature.

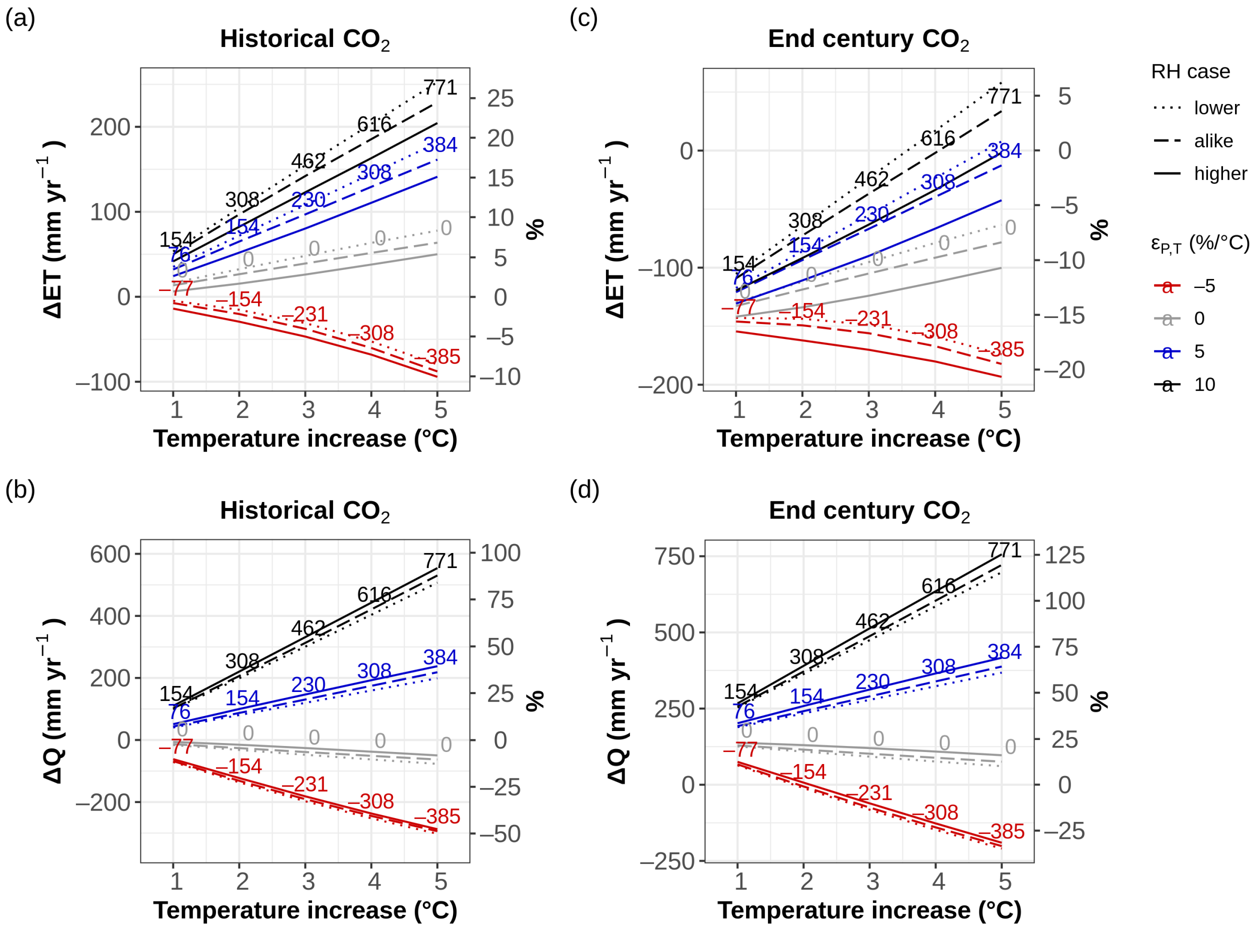

Figure 7. Hydrological responses of ET and Q shown as differences of experiment minus control simulation (ET, Panels (**a**,**c**)) and specific discharge (Q, Panels (**b**,**d**)), in mm yr^{-1} (left *y*-axis) and percentage variation (right *y*-axis), forced by: temperature increase (*x*-axis, in °C); elasticity of precipitation to temperature $\epsilon_{P,T}$, in % °C^{-1} (colors), with actual changes of precipitation displayed as labels, in mm yr^{-1}; changes of relative humidity (RH) with the cases lower (dotted line), alike (dashed line), and higher (solid line); and changes of CO_2 concentration (historical in Panels (**a**,**b**) and end of the century in Panels (**c**,**d**)).

Concerning the changes of ET in the end of the century CO_2 cases (Figure 7c), we noted the prevailing feature of ET reduction, mostly due to the decreasing stomatal conductance and transpiration under a high CO_2 concentration. This notwithstanding, the ET sensitivity to increasing temperature and RH showed similar directions if compared to the historical CO_2 cases. The only pronounced exception was at $\epsilon_{P,T}$ = 10% °C^{-1} (black lines in Figure 7c) at a temperature increase of 5 °C, where ET responded positively. With varying RH, ET responded to temperature similarly to the historical case with changes below 5%. In summary, changes in ET with temperature and RH at the end of the century CO_2 ranged approximately between −15 and −20% (less precipitation case) and −15 and +5% (constant/increasing precipitation cases). Such a dominant pattern of ET reduction led to an overall increase in Q in all cases of end of the century CO_2 (Figure 7d), except for less precipitation case (red lines in Figure 7d). The increases in Q under end of the century CO_2 concentration were higher than those in the historical CO_2 (Figure 7b). These findings are coherent with the concept of the water savings effect in experiments of CO_2 enrichment in deciduous forests [64] and semi-arid grasslands [65]. These changes in Q with temperature and RH ranged approximately between −30 and +10% (less precipitation forcing case) and +10 and 125% (constant/increasing precipitation forcing cases). Interestingly, with less precipitation forcing ($\epsilon_{P,T}$ = −5% °C^{-1}, red lines in Figure 7d), Q increased by about 10% in the 1 °C warmer case, did not alter in the 2 °C case, and kept descending in the warmer cases. That is, for a temperature increase above 2 °C, the growing water gains in the system resulted from descending ET were offset by growing losses of precipitation.

3.3. Comparison of Hydrological Simulations to Observations and Global Models

We compared the boxplot distribution of the current calculations to observational data and CMIP5 GCM ensembles using estimates in each data set as detailed in Figure 8. The median of global models ("CMIP5") underestimated the observed precipitation ("Obs") in the current CO_2 case by about 215 mm yr^{-1} and surprisingly overestimated ET by about 110 mm yr^{-1}, which reflects the disagreement of median ET/P ratio of 0.76 for GCMs and of 0.58 for the observations. As a consequence, the median discharge of global models was about half of the observations. The slightly distinct ranges of calculations between GCMs and observations possibly explain partly those discrepancies. However, the difference of discharges was quite large and likely reflects the strong regional bias of most GCMs to simulate the land water budget, which highlights the relevance of using regional HMs to estimate ET and (P-ET) more accurately.

The changes between historical to end of the century cases of GCMs' median P, ET, and Q were in general low (3%; <1%, −3%, respectively), as suggested by how the models spread their individual differences (Figure 2c) and in agreement with the lack of consensus between models reported by Magrin et al. [31]. With respect to the small changes in ET, Berg and Sheffield [66] showed that a subset of climate models from CMIP5 simulates reduced transpiration rates at the tropics, due to the stomatal closure effect of increased CO_2 on plants, but this difference is offset by increased soil evaporation.

As for the hydrological experiments, the variability of distributions for both ET and Q in a single temperature and also across the ranging temperatures were generally proportional to the correspondent variability of precipitation. The ET inter-quartile variability in the individual experiments was always shorter than the natural one.

So far, we described the distribution of P, ET, and Q as a whole, retaining the discussion to median changes between CMIP5 and the hydrologic model simulations, as well as between the historical and end of the century CO_2 cases.

To analyze the impacts of climate change on the discharge patterns of exceptional anomalous droughts, such as the 2014 one, it is necessary to pay attention to specific events. Therefore, we focused on SWAT-simulated discharge with the perturbed forcing data of 2014.

The 2014 drought event is shown as the bottom outlier (bottom color circles for model P and Q in Figure 8), with some of the Q simulations comparable to the observed discharge. The comparison of this episode is more clearly interpreted from the perspective of the seasonal variability. It was chosen to use a 15-day mean to improve the visualization of the drought minimum at the end of the dry season in October. For the unaltered rainfall ($\epsilon_{P,T}$ = 0% °C^{-1}) and historical CO_2 case (Figure 9-top right), the calculated discharges showed little variation with temperature and were, in general, close to the observations.

Subsequently, for the end of the century CO_2 case (Figure 9, bottom right), we noted that the sensitivity of discharge to temperature was alike low, and the simulations in the wet season were well above the observations, but the observed low flows during July to November were overestimated by about 1 m^3 s^{-1} (or only 5% of the long-term average). In addition, for the decreasing rainfall ($\epsilon_{P,T}$ = -5% °C^{-1} in Figure 9-left), we noted a good agreement between the simulated discharge and the observations and, differently, a substantial sensitivity of discharge to the temperature. Especially for the end of the century CO_2 case (Figure 9-bottom left), despite the highly decreasing ET as affected by stomatal closure, the calculated discharges in the wet season tended to approximate the observations with increasing temperature. For the low flows, they were in general close to the observation for the entire range of temperatures.

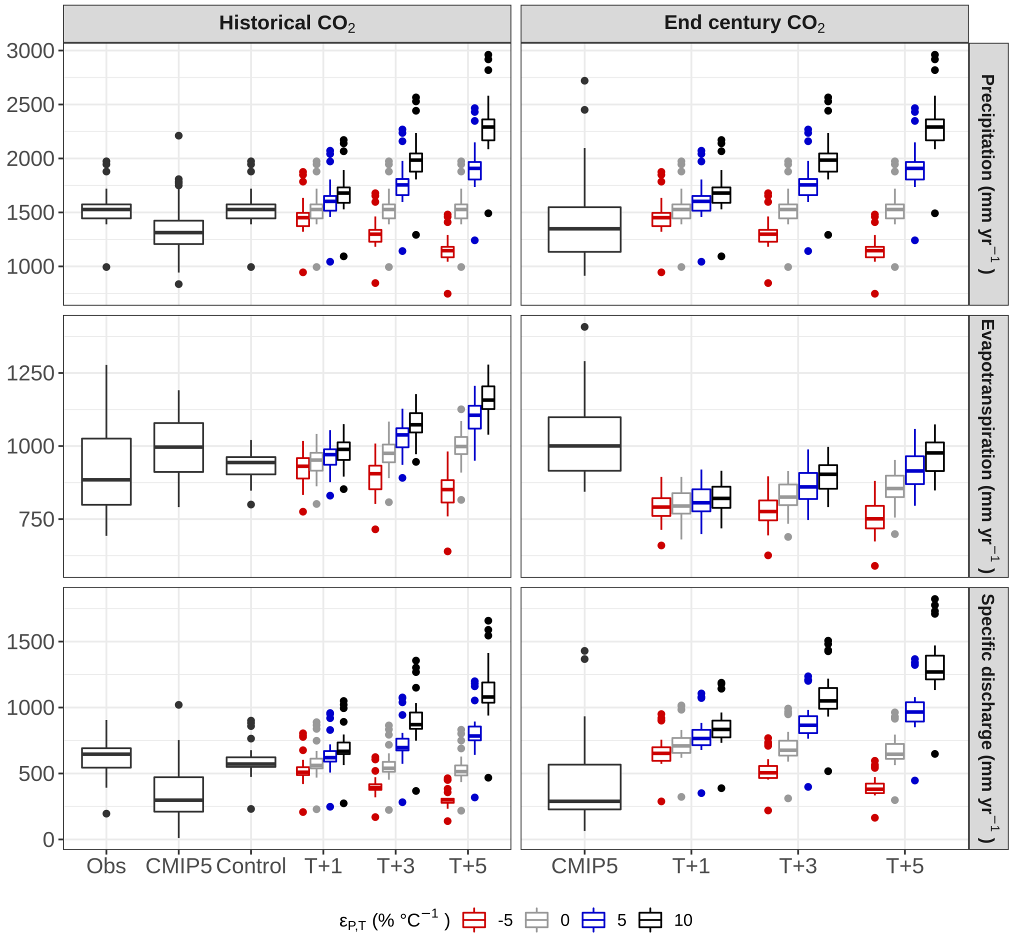

Figure 8. Boxplot distribution of yearly values of P (**top**), ET (**middle**), and Q (**bottom**), all in mm yr^{-1}, with the temporal distribution of observational data (Obs); distribution among CMIP5 model output ensembles (CMIP5); temporal distribution of control simulation (Control); and temporal distribution of current experiments shown for: temperature increase of $T + 1$, $T + 3$, and $T + 5$ °C all for the alike RH case; the elasticity of precipitation to the temperature (-5; 0; 5; 10% °C^{-1}, colors) and CO_2 concentration cases (historical, left column, and end 21st Century, right column). The observations used field water budget with P and Q measures and ET = P-Q; for CMIP5 outputs, the historical (end of the century) CO_2 cases ranged between 1980 and 2004 (2075 and 2099), respectively, in the RCP 8.5 scenario, with estimates of Q = P-ET.

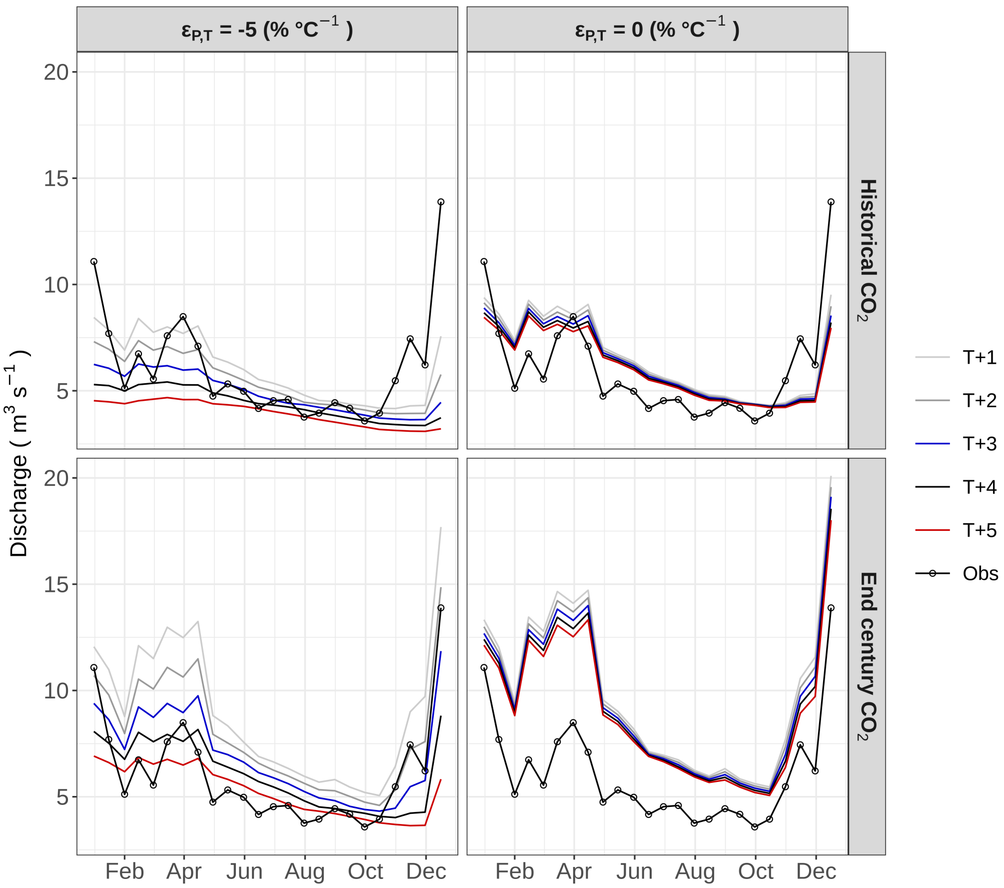

Figure 9. The 15-day mean of 2014 simulated discharge (in $m^3\ s^{-1}$) with temperature increase (colors) and CO_2 concentration (**top** and **bottom** panels) for prescribed changing precipitation of $\epsilon_{P,T}$ = −5% °C^{-1} (**left**) and $\epsilon_{P,T}$ = 0% °C^{-1} (**right**), all for the alike RH case. Observed discharge in 2014 is shown as black line with circles.

4. Conclusions

The outstanding regional drought during 2014/2015 greatly affected the water supply to Southeast Brazil. That caused a water shortage mainly in São Paulo city and raised the concern of how climate change may impact the water budget at the watershed scale. The global climate projections are all confident, showing regional trends with growing temperatures until late 21st Century. However, the projections for rainfall changes were mixed among models, revealing them to be uncertain with a lack of consensus. We prescribed individual elasticities of rainfall and air humidity to temperature, derived from the set of the CMIP5 ensembles, as well as the historical and end of the century CO_2 concentration scenarios, to use forcing–response relationships on a calibrated hydrological model (SWAT) in the Jaguari river basin.

The hydrological model was strategically calibrated firstly by approaching the calculation of evapotranspiration and subsequently for the discharge, consistently, to discuss the impacts emphatically based on these variables. It is believed that both the estimates of the atmospheric models for mean ET and runoff (as of P-ET) were very biased, which the calibration effectively improved.

The experiments showed that for the temperature increasing from 1 to 5 °C, opposite impacts in the future are expected, mostly driven by the simulated variability of rainfall changes. On the one hand, with increasing rainfall, mean ET and Q increased up to +25% and +90%, respectively. On the other hand, with decreasing rainfall, decreases of −10% and −50% were found for mean ET and Q, respectively. Temperature or relative humidity alone played minor roles when compared to rainfall and CO_2 concentration. It was remarkable how future higher CO_2 concentrations strongly decreased the mean ET as affected by decreasing stomatal conductance, which in turn increased the mean Q in near proportions.

It is suggested that major critical impacts for water management be warned with the current results and can be associated to the 2014 drought episode. Even supposing small reductions of precipitation for the future and despite the expectations of decreasing ET, the hydrological simulations replicated the discharge patterns at similar intensities of the drought event.

Overall, the experimental design seemed interesting and easy to interpret, although there were weaknesses that can be improved. An important issue refers to the simulation of extreme events. For example, in places where mean rainfall projected by global atmospheric projections is likely to decrease in the future, so the droughts are likely to increase in frequency and/or length, a pattern that our design did not address accurately. On the other hand, extreme peak discharge in our region of study is often caused by intense hourly basis rainfall and/or continuous rainy days, both of them not exactly met on how precipitation was perturbed.

Additionally, our results did not cover scenarios of land use changes for the end of the century. As the forest formation in the region is protected by Federal Law 11.428/2006, which prohibits deforestation and financially stimulates conservation projects, we assumed afforestation as a possible scenario. Under such a case, we would expect that ET rates may enhance and discharge and water savings reduce, in comparison to the average rates presented in this work, with the magnitude of change depending on the afforestation percentage. However, further investigation is needed to assess in more detail such changes.

Author Contributions: Conceptualization, L.M.D. and H.R.d.R.; methodology, L.M.D., R.C.d.A. and H.R.d.R.; software, L.M.D. and R.C.d.A.; validation, L.M.D.; formal analysis, L.M.D. and R.C.d.A.; investigation, L.M.D.; resources, H.R.d.R.; data curation, L.M.D. and R.C.d.A.; writing—original draft preparation, L.M.D. and H.R.d.R.; writing—review and editing, L.M.D. and H.R.d.R.; visualization, L.M.D.; supervision, L.M.D. and H.R.d.R.; project administration, L.M.D. and H.R.d.R.; funding acquisition, H.R.d.R. All authors have read and agreed to the published version of the manuscript.

Funding: This research was funded by Fundação de Amparo à Pesquisa do Estado de São Paulo (FAPESP) Grant Numbers 2015/50682-6 and 2019/23853-5, Conselho Nacional de Desenvolvimento Científico e Tecnológico (CNPq) Grant Number 446278/2015-7, and Coordenação de Aperfeiçoamento de Pessoal de Nível Superior/Agência Nacional de Águas e Saneamento Básico (CAPES/ANA) Grant Number 88887.144979/2017-00.

Institutional Review Board Statement: Not applicable.

Informed Consent Statement: Not applicable.

Data Availability Statement: The data presented in this study are openly available in Zenodo at https://doi.org/10.5281/zenodo.6456116 (accessed on 17 February 2022).

Acknowledgments: L.M.D. and R.C.d.A. would like to acknowledge CAPES—Finance Code 001 for the studentship grant.

Conflicts of Interest: The authors declare no conflict of interest.

Appendix A. Adjustments in Evapotranspiration

We worked on adjustments of evapotranspiration partition, modifying the parameters listed in Table A1. Parameters BLAI and ALAI_MIN were used to set a fixed seasonal LAI curve, supposing a sinusoidal behavior, according to Equation (A1):

$$\mathrm{LAI}_{i,j} = \mathrm{BLAI}_j - (\mathrm{BLAI}_j - \mathrm{ALAI\_MIN}_j) \cdot \left[0.5 \cdot \left(sin(5.5\pi + \frac{\pi i}{182}) + 1\right)\right]^{1.1} \tag{A1}$$

where indexes i and j represent the day of the year and the land cover, respectively, and 182 is the day of the year when $\mathrm{ALAI\_MIN}_j$ is expected. The LAI curves fit for both pasture and forest land covers are shown in Figure A1.

Table A1. Parameters used in the evapotranspiration adjustment process, for forest and pasture land covers.

	Unit	Forest	Pasture
BLAI Maximum potential leaf area index	m^2m^{-2}	5.2	2.5
ALAI_MIN Minimum leaf area index for plant during dormant period	m^2m^{-2}	4.5	1.0
GSI Maximum stomatal conductance	mm s^{-1}	8.5	1.0
ESCO Soil evaporation compensation factor	-	1.0	1.0
RDMX Maximum root depth	m	2.0	2.0
VPDFR vpd corresponding to the second point on the stomatal curve	kPa	2.0	2.0

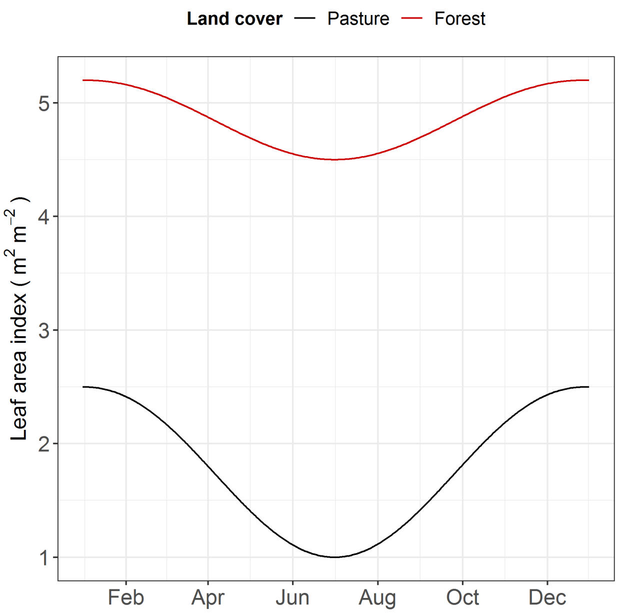

Figure A1. Daily variation of leaf area index, in m^2 m^{-2}, in a year, for pasture (black line) and forest (red line) land covers.

Appendix B. Adjustments in the Drought Flow

With respect to the simulated discharge, drought flows were repeatedly underestimated on the calibration. This happened because the percolation from the bottom soil layer to the shallow aquifer was limited, producing almost no base flow. Seepage to the next layer and lateral flow are calculated individually in the model, and both depends on the drainable water (amount exceeding field capacity) leaving each soil layer. We modified soil parameters (Table A2) to maximize the seepage, without boosting the lateral flow, to improve the representation of drought flows. For simplicity, both LVA and PVA soils were set with the same values in the whole profile.

Table A2. Parameters used to adjust drought flow.

Parameter	Unit	Value
Bulk density	Mg m^{-3}	0.9
Saturated hydraulic conductivity	mm h^{-1}	65
Available water content	-	0.13 [a]

[a] Except in the top layer, which is 0.10 Mg m^{-3}.

Appendix C. Calibration Outputs

Results from the calibration process are summarized in Table A3.

Table A3. Set of model parameters used in the calibration process. The period of variation, default values of the model, and values that optimized the error function (NSE) are also shown. Parameters indicated with prefix *r* were altered percentagewise relative to the original value. Parameters indicated with prefix *a* were altered with values added to the original value. In the remaining parameters, with prefix *v*, the original values were replaced.

Parameter	Definition	Range	Default	Best
r CN2	Curve number at condition II	−40%, 40%	0%	−39.7
v LAT_TTIME	Lateral flow travel time (days)	1.0, 6.0	0.0	4.0
v OV_N	Manning's "n" value for overland flow	0.17, 0.4	0.1	0.36
r HRU_SLP	Average slope of the subbasin (m m^{-1})	−25%, 25%	0%	−15%
v CH_S1	Average slope of tributary channels (m m^{-1})	0.001, 0.055	*	0.010
r SLSUBBSN	Average slope length (m)	−25%, 25%	0%	−2.6%
v CH_S2	Average slope of main channel along the channel length (m m^{-1})	0.001, 0.02	*	0.013
v CH_N2	Manning's "n" value for the main channel	0.025, 0.3	0.014	0.14
v CH_K2	Effective hydraulic conductivity in the main channel alluvium (mm h^{-1})	5, 120	0	36
v RCHRG_DP	Deep aquifer percolation factor	0.0, 0.2	0.05	0.19
v ALPHA_BF	Baseflow recession constant (days)	0.0, 0.1	0.048	0.027
a REVAPMN	Threshold depth of water in the shallow aquifer to revap or percolation do deep aquifer occur (mm)	−500, 0	750	−177
r GW_DELAY	Groundwater delay (days)	−20%, 20%	31	1.8%
v GW_REVAP	Groundwater "revap" coefficient	0.1, 0.5	0.02	0.2
a GWQMN	Threshold depth of water in the shallow aquifer required for base flow to occur (mm)	−100, 100	400	98

* Multiple values are found for the respective parameter.

References

1. Coelho, C.A.S.; de Oliveira, C.P.; Ambrizzi, T.; Reboita, M.S.; Carpenedo, C.B.; Campos, J.L.P.S.; Tomaziello, A.C.N.; Pampuch, L.A.; Custódio, M.d.S.; Dutra, L.M.M.; et al. The 2014 southeast Brazil austral summer drought: Regional scale mechanisms and teleconnections. *Clim. Dyn.* **2016**, *46*, 3737–3752. [CrossRef]
2. Nobre, C.A.; Marengo, J.A.; Seluchi, M.E.; Cuartas, L.A.; Alves, L.M. Some Characteristics and Impacts of the Drought and Water Crisis in Southeastern Brazil during 2014 and 2015. *J. Water Resour. Prot.* **2016**, *8*, 252–262. [CrossRef]
3. Milano, M.; Reynard, E.; Muniz-Miranda, G.; Guerrin, J. Water Supply Basins of São Paulo Metropolitan Region: Hydro-Climatic Characteristics of the 2013–2015 Water Crisis. *Water* **2018**, *10*, 1517. [CrossRef]
4. Millington, N. Producing water scarcity in São Paulo, Brazil: The 2014–2015 water crisis and the binding politics of infrastructure. *Polit. Geogr.* **2018**, *65*, 26–34. [CrossRef]
5. Escobar, H. Drought triggers alarms in Brazil's biggest metropolis. *Science* **2015**, *347*, 812. [CrossRef]
6. Otto, F.E.L.; Haustein, K.; Uhe, P.; Coelho, C.A.S.; Aravequia, J.A.; Almeida, W.; King, A.; Coughlan de Perez, E.; Wada, Y.; van Oldenborgh, G.; et al. Factors Other Than Climate Change, Main Drivers of 2014/15 Water Shortage in Southeast Brazil. *Bull. Am. Meteorol. Soc.* **2016**, *96*, S35–S40. [CrossRef]
7. IPCC. Summary for Policymakers. In *Climate Change 2021: The Physical Science Basis. Contribution of Working Group I to the Sixth Assessment Report of the Intergovernmental Panel on Climate Change*; Masson-Delmotte, V., Zhai, P., Pirani, A., Connors, S., Péan, C., Berger, S., Caud, N., Chen, Y., Goldfarb, L., Gomis, M., et al., Eds.; Cambridge University Press: Cambridge, MA, USA, 2021; *in press*.
8. He, C.; Liu, Z.; Wu, J.; Pan, X.; Fang, Z.; Li, J.; Bryan, B.A. Future global urban water scarcity and potential solutions. *Nat. Commun.* **2021**, *12*, 4667. [CrossRef]
9. Leavesley, G. Modeling the effects of climate change on water resources—A review. *Clim. Chang.* **1994**, *28*, 159–177. [CrossRef]
10. Teng, J.; Chiew, F.H.S.; Vaze, J.; Marvanek, S.; Kirono, D.G.C. Estimation of Climate Change Impact on Mean Annual Runoff across Continental Australia Using Budyko and Fu Equations and Hydrological Models. *J. Hydrometeorol.* **2012**, *13*, 1094–1106. [CrossRef]
11. Creed, I.F.; Spargo, A.T.; Jones, J.A.; Buttle, J.M.; Adams, M.B.; Beall, F.D.; Booth, E.G.; Campbell, J.L.; Clow, D.; Elder, K.; et al. Changing forest water yields in response to climate warming: Results from long-term experimental watershed sites across North America. *Glob. Chang. Biol.* **2014**, *20*, 3191–3208. [CrossRef]
12. Held, I.M.; Soden, B.J. Robust Responses of the Hydrological Cycle to Global Warming. *J. Clim.* **2006**, *19*, 5686–5699. [CrossRef]
13. Byrne, M.P.; O'Gorman, P.A. Understanding Decreases in Land Relative Humidity with Global Warming: Conceptual Model and GCM Simulations. *J. Clim.* **2016**, *29*, 9045–9061. [CrossRef]
14. Guo, D.; Westra, S.; Maier, H.R. Sensitivity of potential evapotranspiration to changes in climate variables for different Australian climatic zones. *Hydrol. Earth Syst. Sci.* **2017**, *21*, 2107–2126. [CrossRef]
15. Ainsworth, E.A.; Rogers, A. The response of photosynthesis and stomatal conductance to rising [CO_2]: Mechanisms and environmental interactions. *Plant Cell Environ.* **2007**, *30*, 258–270. [CrossRef]
16. Purcell, C.; Batke, S.P.; Yiotis, C.; Caballero, R.; Soh, W.K.; Murray, M.; Mcelwain, J.C. Increasing stomatal conductance in response to rising atmospheric CO_2. *Ann. Bot.* **2018**, *121*, 1137–1149. [CrossRef]
17. Milly, P.; Dunne, K. Potential evapotranspiration and continental drying. *Nat. Clim. Chang.* **2016**, *6*, 946–949. [CrossRef]
18. Habermann, E.; Martin, J.A.B.S.; Contin, D.R.; Bossan, V.P.; Barboza, A.; Braga, M.R.B.; Groppo, M.; Martinez, C.A. Increasing atmospheric CO_2 and canopy temperature induces anatomical and physiological changes in leaves of the C4 forage species *Panicum maximum*. *PLoS ONE* **2019**, *14*, e0212506. [CrossRef]
19. Betts, R.A.; Boucher, O.; Collins, M.; Cox, P.M.; Falloon, P.D.; Gedney, N.; Hemming, D.L.; Huntingford, C.; Jones, C.D.; Sexton, D.M.H.; et al. Projected increase in continental runoff due to plant responses to increasing carbon dioxide. *Nature* **2007**, *448*, 1037–1041. [CrossRef]
20. Prudhomme, C.; Giuntoli, I.; Robinson, E.L.; Clark, D.B.; Arnell, N.W.; Dankers, R.; Fekete, B.M.; Franssen, W.; Gerten, D.; Gosling, S.N.; et al. Hydrological droughts in the 21st century, hotspots and uncertainties from a global multimodel ensemble experiment. *Proc. Natl. Acad. Sci. USA* **2014**, *111*, 3262–3267. [CrossRef]
21. Di Baldassarre, G.; Elshamy, M.; van Griensven, A.; Soliman, E.; Kigobe, M.; Ndomba, P.; Mutemi, J.; Mutua, F.; Moges, S.; Xuan, Y.; et al. Future hydrology and climate in the River Nile basin: A review. *Hydrol. Sci. J.* **2011**, *56*, 199–211. [CrossRef]
22. Fowler, H.J.; Blenkinsop, S.; Tebaldi, C. Linking climate change modelling to impacts studies: Recent advances in downscaling techniques for hydrological modelling. *Int. J. Climatol.* **2007**, *27*, 1547–1578. [CrossRef]
23. Xu, C. Climate Change and Hydrologic Models: A Review of Existing Gaps and Recent Research Developments. *Water Resour. Manag.* **1999**, *13*, 369–392. [CrossRef]
24. Wilby, R.L.; Harris, I. A framework for assessing uncertainties in climate change impacts: Low-flow scenarios for the River Thames, UK. *Water Resour. Res.* **2006**, *42*, 2. [CrossRef]
25. Döll, P.; Trautmann, T.; Gerten, D.; Schmied, H.M.; Ostberg, S.; Saaed, F.; Schleussner, C.F. Risks for the global freshwater system at 1.5 °C and 2 °C global warming. *Environ. Res. Lett.* **2018**, *13*, 044038. [CrossRef]
26. Nakicenovic, N.; Alcamo, J.; Grubler, A.; Riahi, K.; Roehrl, R.; Rogner, H.H.; Victor, N. *Special Report on Emissions Scenarios (SRES), A Special Report of Working Group III of the Intergovernmental Panel on Climate Change*; Cambridge University Press: Cambridge, MA, USA, 2000.

27. van Vuuren, D.P.; Edmonds, J.; Kainuma, M.; Riahi, K.; Thomson, A.; Hibbard, K.; Hurtt, G.C.; Kram, T.; Krey, V.; Lamarque, J.F.; et al. The representative concentration pathways: An overview. *Clim. Chang.* **2011**, *109*, 5–31. [CrossRef]
28. Riahi, K.; van Vuuren, D.P.; Kriegler, E.; Edmonds, J.; O'Neill, B.C.; Fujimori, S.; Bauer, N.; Calvin, K.; Dellink, R.; Fricko, O.; et al. The Shared Socioeconomic Pathways and their energy, land use, and greenhouse gas emissions implications: An overview. *Glob. Environ. Chang.* **2017**, *42*, 153–168. [CrossRef]
29. Arnell, N.W. Uncertainty in the relationship between climate forcing and hydrological response in UK catchments. *Hydrol. Earth Syst. Sci.* **2011**, *15*, 897–912. [CrossRef]
30. Xu, H.; Taylor, R.G.; Xu, Y. Quantifying uncertainty in the impacts of climate change on river discharge in sub-catchments of the Yangtze and Yellow River Basins, China. *Hydrol. Earth Syst. Sci.* **2011**, *15*, 333–344. [CrossRef]
31. Magrin, G.O.; Marengo, J.A.; Boulanger, J.P.; Buckeridge, M.S.; Castellanos, E.; Poveda, G.; Scarano, V. Central and South America. In *Climate Change 2014: Impacts, Adaptation, and Vulnerability. Part B: Regional Aspects. Contribution of Working Group II to the Fifth Assessment Report of the Intergovernmental Panel on Climate Change*; Barros, V., Field, C., Dokken, D., Mastrandrea, M., Mach, K., Bilir, T., Chatterjee, M., Ebi, K., Estrada, Y., Genova, R., et al., Eds.; Cambridge University Press: Cambridge, UK; New York, NY, USA, 2014; pp. 1499–1566.
32. Kelman, J. Water Supply to the Two Largest Brazilian Metropolitan Regions. *Aquat. Procedia* **2015**, *5*, 13–21. [CrossRef]
33. Gassman, P.W.; Reyes, M.R.; Green, C.H.; Arnold, J.G. The Soil and Water Assessment Tool: Historical development, applications, and future research directions. *Trans. ASAE* **2007**, *50*, 1211–1250. [CrossRef]
34. Neitsch, S.; Arnold, J.; Kiniry, J.; Williams, J. Soil & Water Assessment Tool Theoretical Documentation Version 2009. *Tex. Water Resour. Inst.* **2011**, *543*, 591–600. [CrossRef]
35. Alaska Satellite Facility Distributed Active Archive Center—ASF DAAC. ALOS PALSAR Radiometric Terrain Corrected Low Res. 2015. Available online: https://asf.alaska.edu/data-sets/derived-data-sets/alos-palsar-rtc/alos-palsar-radiometric-terrain-correction/ (accessed on 30 April 2018).
36. Brazilian Institute of Geography and Statistics—IBGE. *Vector File of Brazilian Land Cover and Land Use for 2012*; IBGE: Rio de Janeiro, Brazil 2015.
37. Federal University of Viçosa—UFV; Minas Gerais Technological Center Foundation—CETEC; Federal University of Lavras—UFLA; State Environment Foundation—FEAM. Soil Map from Minas Gerais State. 2010. Available online: http://www.feam.br/noticias/1/949-mapas-de-solo-do-estado-de-minas-gerais (accessed on 15 April 2018).
38. Dee, D.P.; Uppala, S.M.; Simmons, A.J.; Berrisford, P.; Poli, P.; Kobayashi, S.; Andrae, U.; Balmaseda, M.A.; Balsamo, G.; Bauer, P.; et al. The ERA-Interim reanalysis: Configuration and performance of the data assimilation system. *Q. J. R. Meteorol. Soc.* **2011**, *137*, 553–597. [CrossRef]
39. Pebesma, E.J. Multivariable geostatistics in S: The gstat package. *Comput. Geosci.* **2004**, *30*, 683–691. [CrossRef]
40. Souza, C.M.; Shimbo, J.; Rosa, M.R.; Parente, L.L.; Alencar, A.; Rudorff, B.F.T.; Hasenack, H.; Matsumoto, M.; Ferreira, L.; Souza-Filho, P.W.M.; et al. Reconstructing Three Decades of Land Use and Land Cover Changes in Brazilian Biomes with Landsat Archive and Earth Engine. *Remote Sens.* **2020**, *12*, 2735. [CrossRef]
41. Pontes, L.M.; Viola, M.R.; Silva, M.L.N.; Bispo, D.F.A.; Curi, N. Hydrological modeling of tributaries of Cantareira System, Southeast Brazil, with the SWAT model. *Eng. Agríc.* **2016**, *4430*, 1037–1049. [CrossRef]
42. Thoning, K.; Crotwell, A.; Mund, J. *Atmospheric Carbon Dioxide Dry Air Mole Fractions from continuous measurements at Mauna Loa, Hawaii, Barrow, Alaska, American Samoa and South Pole. 1973–2019*; National Oceanic and Atmospheric Administration (NOAA), Global Monitoring Laboratory (GML): Boulder, CO, USA, 2020. [CrossRef]
43. Basic Sanitation Company of the State of São Paulo—SABESP. Historical Time Series of Rainfall and Streamflow Data. 2018. Available online: https://mananciais.sabesp.com.br/HistoricoSistemas (accessed on 1 June 2018).
44. Strauch, M.; Bernhofer, C.; Koide, S.; Volk, M.; Lorz, C.; Makeschin, F. Using precipitation data ensemble for uncertainty analysis in SWAT streamflow simulation. *J. Hydrol.* **2012**, *414–415*, 413–424. [CrossRef]
45. Mota da Silva, J. The Hydrological Environment Service from Permanent Preservation Areas: A Case Study with Small and Mesoscale Numerical Modeling from Piracicaba River Watershed. Ph.D. Thesis, University of São Paulo, São Paulo, Brazil, 2013.
46. Rafee, S.A.A.; Uvo, C.B.; Martins, J.A.; Domingues, L.M.; Rudke, A.P.; Fujita, T.; Freitas, E.D. Large-Scale Hydrological Modelling of the Upper Paraná River Basin. *Water* **2019**, *11*, 882. [CrossRef]
47. Abbaspour, K.C. SWAT-CUP: SWAT Calibration and Uncertainty Programs—A User Manual. 2015. Available online: https://swat.tamu.edu/media/114860/usermanual_swatcup.pdf (accessed on 1 June 2017).
48. Schürz, C. SWATplusR: Running SWAT2012 and SWAT+ Projects in R; R Package Version 0.2.7. 2019. Available online: https://zenodo.org/record/3373859#.YleLuLYzaUk (accessed on 1 June 2017). [CrossRef]
49. R Core Team. *R: A Language and Environment for Statistical Computing*; R Foundation for Statistical Computing: Vienna, Austria, 2013.
50. Taylor, K.E.; Stouffer, R.J.; Meehl, G.A. An Overview of CMIP5 and the Experiment Design. *Bull. Am. Meteorol. Soc.* **2012**, *93*, 485–498. [CrossRef]
51. Miralles, D.G.; Holmes, T.R.H.; De Jeu, R.A.M.; Gash, J.H.; Meesters, A.G.C.A.; Dolman, A.J. Global land-surface evaporation estimated from satellite-based observations. *Hydrol. Earth Syst. Sci.* **2011**, *15*, 453–469. [CrossRef]
52. Mu, Q.; Zhao, M.; Running, S.W. Improvements to a MODIS global terrestrial evapotranspiration algorithm. *Remote Sens. Environ.* **2011**, *115*, 1781–1800. [CrossRef]

53. Dirmeyer, P.A.; Gao, X.; Zhao, M.; Guo, Z.; Oki, T.; Hanasaki, N. GSWP-2: Multimodel Analysis and Implications for Our Perception of the Land Surface. *Bull. Am. Meteorol. Soc.* **2006**, *87*, 1381–1397. [CrossRef]
54. Zhang, K.; Kimball, J.S.; Nemani, R.R.; Running, S.W. A continuous satellite-derived global record of land surface evapotranspiration from 1983 to 2006. *Water Resour. Res.* **2010**, *46*, 8800. [CrossRef]
55. Liu, W.; Wang, L.; Zhou, J.; Li, Y.; Sun, F.; Fu, G.; Li, X.; Sang, Y.F. A worldwide evaluation of basin-scale evapotranspiration estimates against the water balance method. *J. Hydrol.* **2016**, *538*, 82–95. [CrossRef]
56. da Rocha, H.R.; Manzi, A.O.; Cabral, O.M.; Miller, S.D.; Goulden, M.L.; Saleska, S.R.; Coupe, N.; Wofsy, S.C.; Borma, L.S.; Artaxo, P.; et al. Patterns of water and heat flux across a biome gradient from tropical forest to savanna in Brazil. *J. Geophys. Res.* **2009**, *114*, G00B12. [CrossRef]
57. Save, H.; Bettadpur, S.; Tapley, B.D. High-resolution CSR GRACE RL05 Mascons. *J. Geophys. Res. Solid Earth* **2016**, *121*, 7547–7569. [CrossRef]
58. Moriasi, D.N.; Gitau, M.W.; Pai, N.; Daggupati, P. Hydrologic and Water Quality Models: Performance Measures and Evaluation Criteria. *Trans. ASABE* **2015**, *58*, 1763–1785. [CrossRef]
59. Krause, P.; Boyle, D.P.; Bäse, F. Comparison of different efficiency criteria for hydrological model assessment. *Adv. Geosci.* **2005**, *5*, 89–97. [CrossRef]
60. Althoff, D.; Rodrigues, L.N. Goodness-of-fit criteria for hydrological models: Model calibration and performance assessment. *J. Hydrol.* **2021**, *600*, 126674. [CrossRef]
61. Zheng, F.; Maier, H.R.; Wu, W.; Dandy, G.C.; Gupta, H.V.; Zhang, T. On Lack of Robustness in Hydrological Model Development Due to Absence of Guidelines for Selecting Calibration and Evaluation Data: Demonstration for Data-Driven Models. *Water Resour. Res.* **2018**, *54*, 1013–1030. [CrossRef]
62. Nguyen, V.T.; Dietrich, J. Modification of the SWAT model to simulate regional groundwater flow using a multicell aquifer. *Hydrol. Process.* **2018**, *32*, 939–953. [CrossRef]
63. Bonan, G. *Ecological Climatology: Concepts and Applications*, 3rd ed.; Cambridge University Press: Cambridge, MA, USA, 2015. [CrossRef]
64. Leuzinger, S.; Körner, C. Water savings in mature deciduous forest trees under elevated CO_2. *Glob. Chang. Biol.* **2007**, *13*, 2498–2508. [CrossRef]
65. Morgan, J.A.; LeCain, D.R.; Pendall, E.; Blumenthal, D.M.; Kimball, B.A.; Carrillo, Y.; Williams, D.G.; Heisler-White, J.; Dijkstra, F.A.; West, M. C4 grasses prosper as carbon dioxide eliminates desiccation in warmed semi-arid grassland. *Nature* **2011**, *476*, 202–205. [CrossRef]
66. Berg, A.; Sheffield, J. Evapotranspiration Partitioning in CMIP5 Models: Uncertainties and Future Projections. *J. Clim.* **2019**, *32*, 2653–2671. [CrossRef]